Nanoparticle Size Influences the Self-Assembly of Gold Nanorods Using Flexible Streptavidin-Biotin Linkages

Maegen Kincanon and Catherine J. Murphy*

Department of Chemistry, 600. S. Mathews Ave., University of Illinois at Urbana-Champaign, Urbana, Illinois 61801, USA.

*to whom correspondence should be addressed: murphycj@illinois.edu; 1-217-333-7680.

ABSTRACT

The self-assembly of colloidal nanocrystals remains of robust interest due to its potential in creating hierarchical nanomaterials that have advanced function. For gold nanocrystals, junctions between nanoparticles yield large enhancements in local electric fields under resonant illumination, suitable for surface-enhanced spectroscopies for molecular sensors. Gold nanorods can provide such plasmonic fields at near-infrared wavelengths of light for longitudinal excitation. Through use of careful concentration and stoichiometric control, a method is reported herein for selective biotinylation of the ends of gold nanorods for simple, consistent, and high-yielding self-assembly upon addition of the biotin-binding protein streptavidin. This method was applied to four different sized nanorods of similar aspect ratio and analyzed through UV-vis spectroscopy for qualitative confirmation of self-assembly, and transmission electron microscopy to determine the degree of self-assembly in end-linked nanorods. The yield of end-linked assemblies approaches 90% for the largest nanorods and approaches 0% for the smallest nanorods. The number of nanorods linked in one chain also increases with increased nanoparticle size. The results support the notion that the lower ligand density at the ends of the larger nanorods yields preferential substitution reactions at those ends and hence preferential end-to-end assembly, while the smallest nanorods have relatively uniform ligand density across their surfaces, leading to spatially random substitution reactions.

Keywords: gold nanorods, ligand density, self-assembly, selective functionalization, biotin, streptavidin

TOC

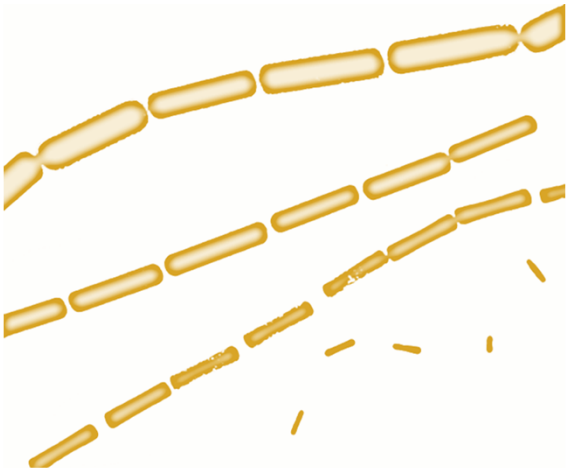

Gold nanorods (AuNRs) are appealing materials for optical sensors due to their plasmonic properties,[1] which can be tuned by their size, shape, and surface functionalization.[2] AuNRs are well known to exhibit both transverse and longitudinal plasmon bands, where the difference in the extinction cross sections along the two axes leads to substantially stronger electromagnetic field enhancements at the ends of the NRs upon appropriate illumination.[3-5] When two or more NRs are brought into close proximity and their ends align, they create interparticle junctions with amplified electric field strengths between the two ends, known as second-generation hot spots.[1,3] These hot spots result from the coupling of the individual NRs' surface plasmons[6] and combine distinct spatial and angular photoexcitation distributions[7-9] that intensify electromagnetic fields.[5,10,11] The resultant amplification at the second-generation hot spots has been utilized for signal enhancement of analytes as the analytes interact with these nanogaps.[1,5,12,13] This amplification process holds great efficacy in nanoengineering of devices for sensing, imaging, waveguides, and catalysis, among others.[2] The increased intensity of the electromagnetic fields allows for lower limits of detection for fluorescence,[12] luminescence,[14] or other techniques that utilize plasmonic enhancement.[15]

Self-assembly offers a facile way of generating second-generation hot spots through either top-down or bottom-up assembly processes. Top-down approaches may involve the use of lithography,[16,17] nanoline-gaps,[18] electrodes,[19] shadow-sphere,[20] hydrophobic surfaces,[21] capillaries,[22] template-assisted,[23] templated dewetting,[24] electrochemistry,[25] or other techniques[26-29] to facilitate the alignment of nanoparticles. In contrast, a bottom-up approach utilizes the surface ligands of the NRs for self-assembly through DNA cross-linking,[30-34] DNA with thiol groups,[34,35] biotin-streptavidin interactions,[36,37] cooperative hydrogen bonding,[38] or proteins.[39,40] As a solution-phase approach, solvent properties can alter how nanoparticles assemble by tuning their electric field strength and interactions.[41] For instance, thermodynamic generation of patchy nanoparticles, as shown by Kumacheva and coworkers,[41] achieved highly controlled tethering of nanoparticles by controlling the polymer-solvent interactions. Between these techniques, numerous processes for the formation of either vertically[13,19,32] or horizontally[12,30-40] aligned NRs have been developed. A bottom-up approach is more efficient and favorable for comparative exploration of how specific parameters, such as nanoparticle size, shape, ligand length, or ligand type, can influence the stages of the self-assembly process.

However, the major limitations in bottom-up approaches are the lack of reproducibility, low yield, and minimal control over the process.[3,18,42,43] Mixtures of both end-to-end, end-to-side, and side-by-side assembles within colloidal solution are typically observed, and within that mixture the percentage of the sample that undergoes self-assembly is low.[36,37,44] Additionally, the formation and distribution of dimers, trimers, tetramers, or longer chains are often unreproducible and uncontrollable.[18,36,37,44] Thus, there is a need for more control over the self-assembly process, either during the stage in which surface ligands are exchanged for ligands that can participate in self-assembly or during the assembly stage itself. In previous end-to-end self-assembly studies by Niehues *et al*., it was shown that thiols favor end-functionalization.[45] To deduce why end-functionalization would occur before side-functionalization, Carbó-Argibay *et al*. analyzed the crystalline structure of AuNRs to suggest that the difference in crystallinity at the ends and sides of the NR provide different energetic potentials.[46] Ligand density studies by Janicek *et al*. showed that ligand density is significantly lower at the ends of "larger" nanorods than the sides, making functionalization at the ends kinetically more favorable – although smaller nanorods did not show a spatial dependence of ligand density.[47] Hence, with both a thermodynamic and kinetic bias towards end-functionalization, control over the self-assembly process could be applied through careful functionalization of only the ends of the NRs and not the sides, for the appropriate size of nanorod.

In this work we aim to reveal the influence NR absolute size has on the self-assembly process using an array of four distinct NR sizes. If the results of differential ligand density on the end vs. the sides of nanorods are correct, then the prediction would be that the same self-assembly chemistry that is successful for larger nanorods would fail for smaller nanorods.

RESULTS/ DISCUSSION

Self-assembly of anisotropic nanomaterials has proven to be a significant challenge due to limited knowledge surrounding the dynamics of the self-assembly process[43,48] and the consequent lack of control over assembly.[3,42,43] However, if ligand density is lower at the ends of the NRs compared to the sides, as suggested by Carbó-Argibay *et al*. and Janicek *et al.*, control of the self-assembly process would be possible by exploiting the different capacity in which ligand substitution can occur at the ends and sides of the NR.[46,47] Implication of selective end-to-end assembly should, thus, be obtainable.

With the possibilities of NR alignments being end-to-end, end-to-side, and side-to-side, it was essential to bias self-assembly towards one in order to induce control, reliability, and reproducibility of their alignment. Due to the enhanced hot-spot intensity of end-to-end interactions, it would be desirable to favor end-to-end linkages.[1,5,12,13] This should be possible since it is well known that the ligand density of the initial surfactant coating of cetyltrimethylammonium bromide (CTAB) on the NRs depends on the local curvature for NRs.[44,47,49,50] In a comparative study by Janicek *et al.* on two different sizes of rods, it was discovered that there exists a 30% decrease in ligand density at the ends of the NRs of size 45 $\pm$ 5 nm by 15 $\pm$ 2 nm (small NRs) but relatively no difference in ligand density around the surface of NRs of size 31 $\pm$ 5 nm by 11 $\pm$ 2 nm (mini NRs).[47] Hence, it is expected that substitution reactions relying on CTAB displacement ought to yield functionalization chemistry that is also spatially dependent. Choosing nanoparticle size as the experimental parameter, we sought to uncover its influence on the self-assembly process. We used a bottom-up approach utilizing biotin-streptavidin bonding to link the nanorods, due to its specificity, gap lengths of approximately 5 nm,[36] and low equilibrium dissociation constant of $K_D = 10^{15}$ mol^{-1}.[51] Since thiols and disulfides both bind to gold to create Au-S bonds, we decided to covalently attach biotin to a thiol-based ligand (biotin-PEG-SH, 2000 Da molecular weight) or a disulfide-based ligand (biotin-PEG-S-S-PEG-biotin, 4000 Da molecular weight), which ought to effectively displace the CTAB on the ends of the NRs and provide a molecular attachment point for streptavidin. With ligand density of CTAB lower at the ends, it would be expected that displacement should occur at the ends of NRs before the sides, and anisotropic coverage could be tuned with the correct ratio of AuNRs to displacing ligands. We anticipated that this strategy would achieve a high-yielding end-to-end self-assembly process for all NR sizes except mini NRs, which have absolute sizes suggestive of an isotropic CTAB distribution by Janicek *et al*.[47] Moreover, the use of flexible ligands such as 2000 Da biotin-PEG-SH, as opposed to small rigid biotin-thiols, is expected to allow for more facile assembly kinetics.[52]

With a presumed decrease in ligand packing at the ends of NRs as NR size is increased, the hypothesis is that a decrease in selective end-functionalization for the smallest rods would be observed. Four different NR sizes were employed for our comparative study to observe the size dependence of CTAB displacement and self-assembly over a wide range of surface curvatures. We began by synthesizing stock solutions of mini (34 $\pm$ 7 × 6.3 $\pm$ 0.8 nm),[53] small (89 $\pm$ 8 × 19 $\pm$ 2 nm),[54] medium (112 $\pm$ 8 × 26 $\pm$ 1 nm),[15] and large (151 $\pm$ 9 × 39 $\pm$ 2 nm)[15] AuNRs, which exhibited longitudinal surface plasmon resonance bands at 903 nm, 938 nm, 918 nm, and 911 nm, respectively (Figure 1).

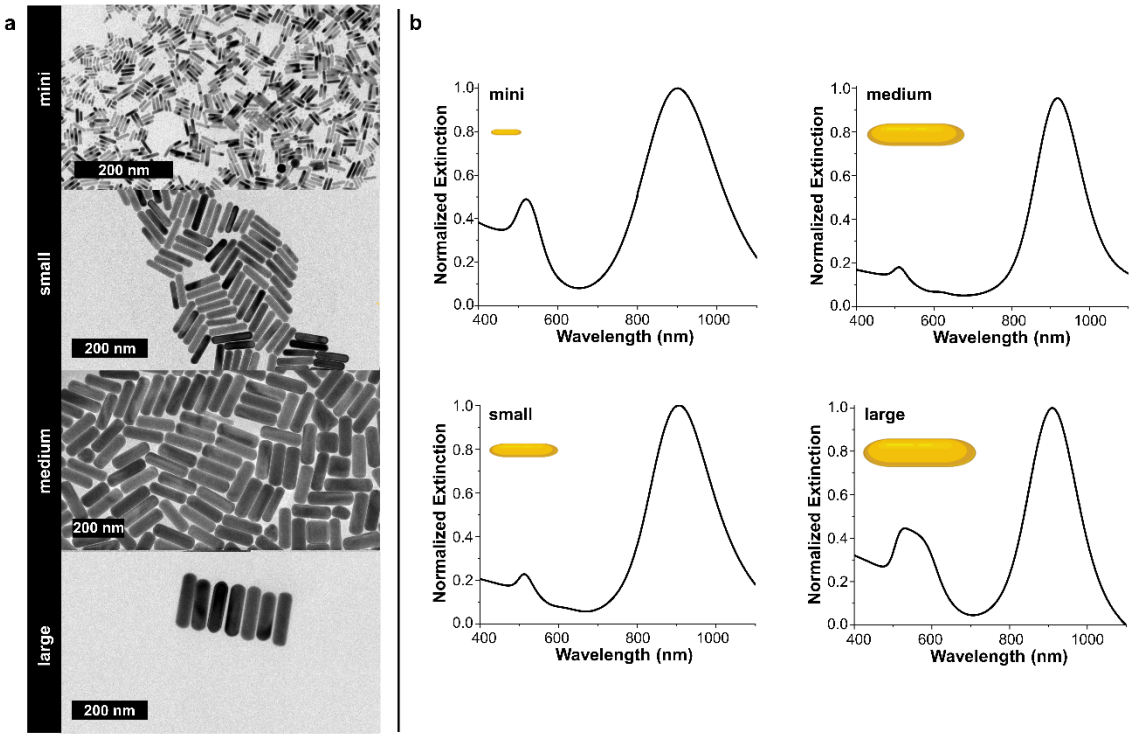

Figure 1. (a) Transmission electron microscopy images and (b) extinction spectra of CTAB-coated gold nanorods before PEGylation, for the four absolute sizes of nanorods. Scale bars = 200 nm for mini, small, medium, and large NRs.

Next, we began the process of selectively coating the ends of the NRs with biotin (Scheme 1), where the plasmonic hot spots are localized upon longitudinal excitation. Selective end-functionalization was undertaken with a thiol-based biotin ligand, as well as the disulfide-based biotin ligand as a presumed control due to increased CTAB end displacement specificity.[55] With the density of the original CTAB coating on AuNRs known to have decreased density at the ends of the NRs for sufficiently large NRs,[44,49,50] we expected to achieve end-selective functionalization for all NRs except the mini NRs. In principle, the reaction that would occur at the gold surface is

$$\text{Au-Br}^- + \text{RSH} \rightarrow \text{Au-SR} + \text{Br}^- + \tfrac{1}{2}\text{H}_2\,(\text{g}) \qquad \text{Equation 1}$$

where the chemisorbed bromide is from the CTAB surfactant.[56] To passivate the sides of the NRs, coating of the sides with excess ^{m}PEG-thiol to remove CTAB from the NRs was then undertaken. With a dissociation energy of 44 kcal/mol is required to break an Au-S bond compared to the 28.8 kcal/mol[57] for dissociating the CTAB bilayer from the gold surface,[58] it was improbable that coating the sides with ^{m}PEG-thiol would remove our pre-functionalized biotinylation. Full removal of CTAB is needed to eliminate unfavorable CTAB-streptavidin interactions that may occur during the subsequent addition of streptavidin. As streptavidin can noncovalently bind up to 4 biotin molecules at once, introduction of this protein ought to lead to biotin-streptavidin-biotin-linked NRs.[3,5,12,59]

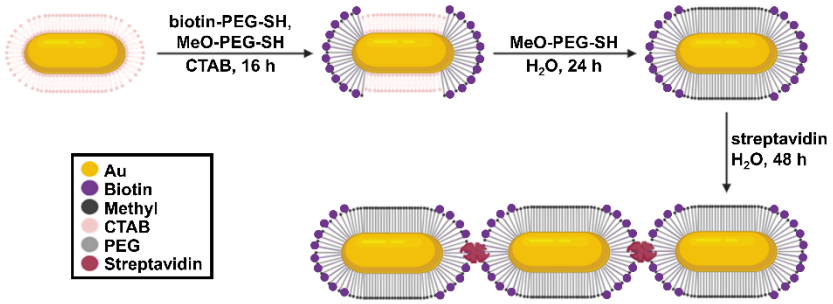

Scheme 1. Synthesis of presumably end-functionalized biotinylated NRs, their methoxyPEG passivation and their self-assembly via streptavidin addition. AuNR, biotin, methyl, PEG, and streptavidin not drawn to scale. For all reagents, nanopure water was used as the solvent with the following reagent concentrations: CTAB (0.1 M), biotin-PEG-SH (0.50 mM, 1:1 ratio with MeO-PEG-SH), MeO-PEG-SH (0.50 mM), and streptavidin (26 nM). NR concentrations for all reactions before addition of streptavidin were 0.125 nM. During addition of streptavidin, NR concentrations were 0.125 nM to 10.00 nM, 0.125 nM, 0.0625 nM, and 0.03215 nM for mini, small, medium, and large NRs respectively.

The medium rods were used to identify conditions of optimal end-to-end linkages of biotinylated NRs upon streptavidin addition. Upon identification of optimal selective end-coating parameters for these medium rods, the amount of end-coating solution was dimensionally scaled to the remaining three NR sizes based on the surface area of the NR end. Total surface area of the NRs was divided into its respective cylindrical and spherical components to represent the sides and ends of the NRs respectively. Surface area calculations of the NR ends were found to be 124.6 nm^2, 1134.1 nm^2, 2123.8 nm^2, and 4778.4 nm^2 for mini, small, medium, and large NRs respectively; the ratios between these numbers relative to the medium rods were used to calculate the amount of biotinylated ligand to add to a given quantity of nanorods for all other nanorod sizes. End-coating was followed by replacing the remaining CTAB with MeO-PEG-SH to eliminate possible interference from CTAB with the streptavidin in the next step. To confirm the presence of biotin on the nanoparticles prior to introducing streptavidin, each nanoparticle sample underwent iodide etching to give an average ligand density of $1.4\pm0.8 \times 10^{15}$, $1.5\pm0.8 \times 10^{16}$, $3.8\pm0.5 \times 10^{16}$, and $6.7\pm0.8 \times 10^{16}$ molecules per NR for mini, small, medium, and large rods respectively. If the NRs are selectively end-coated, based on NR surface area and the calculated area of ligand footprint being between 2-6 nm^2, the number of biotinylated molecules per NR should fall within the range of 1.57×10^{15} to 4.69×10^{15} for mini NRs, 1.42×10^{16} to 4.27×10^{16} for small NRs, 2.66×10^{16} to 7.99×10^{16} for medium NRs, and 5.99×10^{16} to 1.80×10^{17} for large NRs. Comparing these end-coated values to full NR biotinylation values of 1.01×10^{16} to 3.02×10^{16}, 8.09×10^{16} to 2.43×10^{17}, 1.41×10^{17} to 4.24×10^{17}, and 2.92×10^{17} to 8.76×10^{17} molecules per mini, small, medium, and large NRs subsequently, the measured ligand density values generally align with what is predicted for end-selective ligand coating for all but the mini-rods.

After optimizing for preferential end-coating with biotin ligands and passivating the AuNR sides, a solution of streptavidin was added to each NR solution. While it has been reported that self-assembly with a biotin-streptavidin system occurs within 10 minutes when attached to gold[60] or 2 hours when on a biotinylated polymer surface,[61] we allowed our reaction to proceed over 48 hours since a longer reaction time should increase the degree of self-assembly. The optimized reaction conditions for the medium rods were use of 4.00 mL of 0.125 nM NRs, in 0.1 M CTAB with 2.50 µL of a 0.50 mM 1:1 biotin-PEG-SH to ^{m}PEG-SH aqueous solution and agitated for 16 h for selective coating of the NR ends. Side functionalization with excess aqueous 0.50 mM ^{m}PEG-SH solution was then undergone to remove the remaining CTAB from the NRs. Self-assembly was then undergone by mixing 1.00 mL of 0.125 nM AuNRs suspended in water and 100 µL 26 nM aqueous streptavidin together by inverting 3 times, and the mixture was left to age undisturbed for at least 4 h. The reaction was deemed to be ready for analysis once the presumed assembled NRs underwent complete sedimentation to the bottom of the reaction vial.

To assess whether or not self-assembly was successful in a rapid manner, we utilized UV-Vis-NIR extinction measurements. We expected that upon functionalization with streptavidin, the biotinylated

nanorods would assemble end-to-end, and therefore the longitudinal surface plasmon resonance (LSPR) band would red shift, or move to longer wavelengths.[16,33,44,62,63] Indeed, 48 h after the addition of streptavidin, there was a significant red shift of the LSPR wavelength for each of the small, medium, and large rods (Figure 2), ranging from 26 to 42 nm. In principle, Mie theory can estimate the approximate wavelength shift based on the number of NRs in an end-to-end assembly.[26,64,65] A previous study by Abtahi *et al*. utilized a modified, extended version of Mie theory to predict the shift in wavelength during sulfate-mediated self-assembly.[66] According to their calculations, they found an approximate 105 nm red shift occurred upon the addition of each NR, shifting the longitudinal plasmonic maximum wavelength from 756 nm to 860 nm, 964 nm, then 1070 nm for dimers, trimers, and tetramers respectively. Accounting for the difference in single NR LSPR wavelength, the dielectric constants of the surrounding media, and the difference in depolarization factors for our nanorods, we predict a 32 nm red shift as the NRs link together. This prediction suggests that the observed optical spectra result from chains of end-linked nanorods that are dimers through tetramers and beyond (Figure 2).

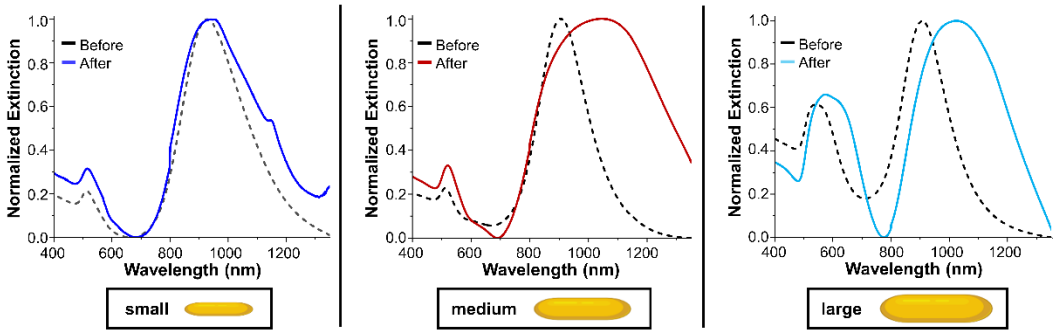

Figure 2. Normalized extinction spectra of small, medium, and large biotinylated nanorods before (dashed line) and after (solid line) the addition of streptavidin. For small NRs, concentrations of 0.0625 nM NR with the addition of 100 µL 26 nM streptavidin were utilized. Medium and large NRs were run at a concentration of 0.0625 nM with 100 µL 26 nM streptavidin and 0.03125 nM with 50 µL streptavidin, respectively. Final spectra were taken, following redispersion of any formed pellet, approximately 48 h after the addition of streptavidin.

Transmission electron microscopy (TEM) allowed for visualization of the self-assembled rods (Figure 3). For each NR condition, TEM analysis was undergone before addition of streptavidin, after addition of streptavidin, and with biotin coating both sides and ends of the NRs. Scanning approximately 75% of the TEM grids, obtaining images from multiple sections to produce the most accurate representation of the samples' degrees of self-assembly and minimizing potential sampling bias, the spacing between NRs, number of NRs linked together, and number of NRs not assembled were quantified. Data was assessed by using a total of six batches per condition with at least 16,000 NRs and at least 10,000 junctions counted per batch. Since one molecule of streptavidin has the dimensions of 4.5 x 4.5 x 5.8 nm^3, we would expect to see a 4-6 nm gap between NRs when self-assembled with streptavidin linkers.[36,44] The 2K biotin-PEG-thiol linker could add a 1-4 nm distance between NRs when conformationally condensed but can reach 12 nm when unraveled. Undergoing a conservative estimation at the shorter end of the range to simplify our measurements, a range of 3-10 nm between particles was considered to be linked together, and any other value between NRs was assumed to not be biotin-streptavidin linked (Figure 4b). Between each of the six batches for each small, medium, and large rods, we observed an average distance of approximately 5 nm. These distances match the expected approximately 5-nm gap that streptavidin would leave between NRs when bound to the biotin on the NR surfaces. These values are significantly different than the spacing between NRs when no streptavidin is added and self-assembly is not expected to occur, with non-assembled spacing ranging between 1-2 nm. However, besides the desired end-to-end self-assembly, we also observe a small amount of end-to-side self-assembly where distances between the end and side of NRs averaged a

gap size of 4.3 ± 0.8 nm for small NRs, 4.4 ± 1.5 nm for medium NRs using thiol for coating, and 5.0 ± 1.0 nm for large NRs.

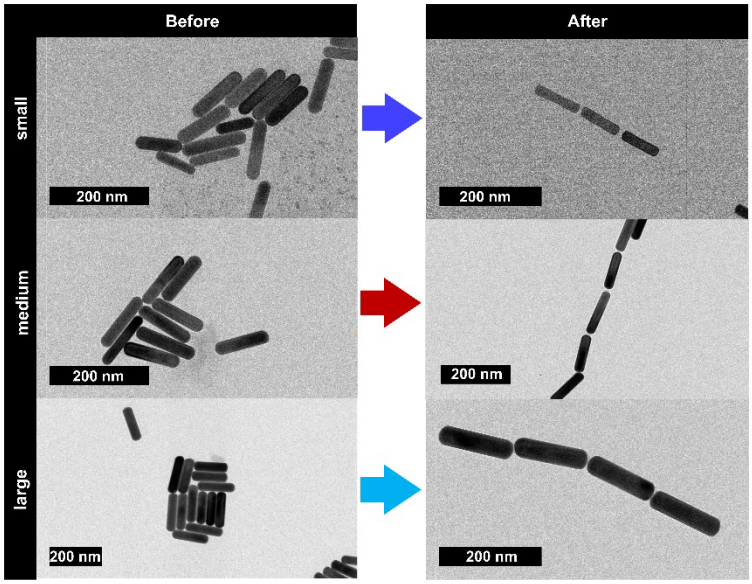

Figure 3. TEM images before (left) and after (right) the addition of streptavidin for small, medium, and large NRs (top to bottom). Scale bars = 200 nm.

Based on the TEM images and corresponding spacing analysis, we were able to determine the percentage of achieved self-assembly that was end-to-end and end-to-side (Figure 4a). Accounting for just the NRs that were within 3-10 nm of other NRs, percentage of end-to-end linkage was 97% for small NRs, 98% for medium NRs, and 99% for large NRs, with the remaining percentages belonging to that of end-to-side linkages. Additionally, despite previous studies by Hinman et al showing that use of a PEG-disulfide is more selective for selectively functionalizing just the ends compared to PEG-thiol,[55] we did not observe a statistically significant difference between any of the small, medium, or large NRs when disulfide was used for coating instead of thiol (see SI for more information). Thus, we hypothesize that the amount of both thiol and disulfide end-coating solutions are optimized to only functionalize the ends of the NRs or that, for rods that are not classified to be mini rods, ability to selectively replace CTAB at the ends of the nanoparticle has minimal difference between thiol and disulfide coating agents (Figure S1). In comparison to our study, previous literature using a biotin-streptavidin assembly method has demonstrated minimal control over favoring end-to-end linkage over end-to-side self-assembly. Gole *et al*. produced an end-to-end linkage of 24% with 59% side-to-side linked,[37] Caswell *et al*. showed an end-to-end linkage of 30% with 34% end-to-side linkage;[36] and Lu *et al*. demonstrate 47% assembly of end-to-end dimers adhered to a glass surface.[44] These methods all display biotinylated ligands coating both the ends and sides of the NRs, lacking chemical control over where the streptavidin may bind.[36,37,44] Our approach selectively localizes biotin to just the ends of the NRs so that side-to-side self-assembly was unable to occur, which in turn depends on adding the appropriate concentration of biotinylated thiol to replace end-located CTAB surfactant. While we did observe a small amount of end-to-side linkage, it was at a much-reduced proportion compared to previous literature. Thus, our protocol has presented itself to be a promising progression to the field of NR self-assembly.

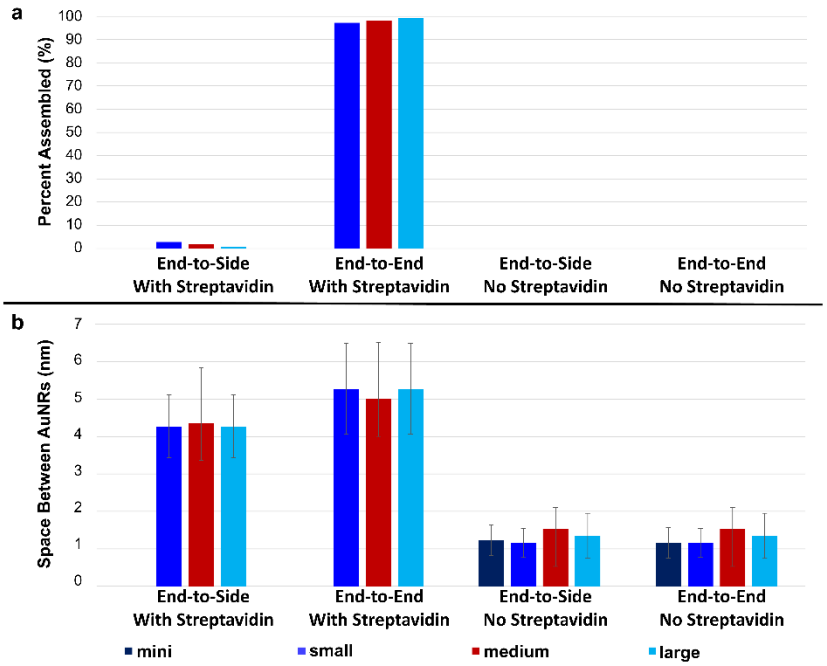

Figure 4. Percentage and average spacing of end-to-side and end-to-end orientations for NRs with addition of streptavidin and without streptavidin, for six different batches of NRs of each size. (a) Percentage of NRs that were end-to-end and end-to-side linked out of all NRs that underwent self-assembly. (b) Average distance between aligned NRs. Error bars represent one standard deviation from the mean.

To determine the limits of the synthetic end-coating methods, a large excess of biotin-PEG-SH solution was added to the NRs by adding 1.00 mL of 0.50 mM biotin-PEG-SH solution to 2.00 mL of 0.125 nM NRs and reacting for 24 h, forming NRs fully coated with biotin. Upon analysis, it was found that the spacing between NRs was also approximately 5 nm (Figure 5b), indicating self-assembly did occur. However, upon analysis of all full-coated NRs participating in NR-NR linkages (Figure 5a), it was found that, besides the large NRs, all sizes yielded an approximate 1:1 ratio between end-to-end and end-to-side coating, which mirrors the results found by Gole[36] and Caswell.[37] With excess biotin-PEG-SH, mini NRs can assemble, albeit without any preference in spatial orientational.

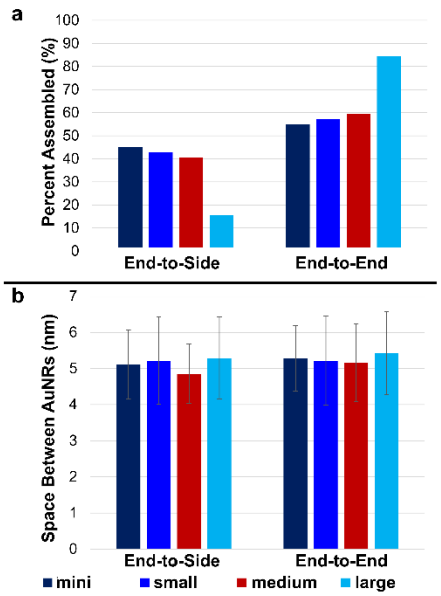

Figure 5. Results of a control study for fully coating NRs with excess biotin-PEG-SH, leading to substitution reactions at all locations along the NRs in principle. (a) Percentage of NRs that were end-to-side and end-to-end linked out of all NRs that underwent self-assembly. (b) Average distance between aligned NRs. Error bars represent one standard deviation from the mean.

The absolute amount of self-assembly was garnered from exhaustive analysis of 16,000 nanorods from multiple batches. Recalculating the end-to-end self-assembly percentage of each condition to include apparently unassembled NRs, the absolute amount of nanorods that self-assemble are 81.0% for small NRs, 92.2% for medium NRs, and 98.2% for large NRs. The trend in overall end-to-end assembly may arise from differences in the percentage of biotin on the ends of each type of NR. During the coating process, the ionic bilayer of CTAB is replaced on the ends of the NRs with a thiol (equation 1). This process is selective towards the ends because CTAB density is lower in comparison to the sides,[44,49,50] which has been seen in a previous study reported by Zijlstra *et al*. that despite the surface area of the sides of their NRs being 3.7 times larger than the surface area of the ends, biotin density was approximately 7 times larger at the ends when a biotinylated ligand was allowed to bind anywhere on the NR surface.[66] Furthermore, inorganic coatings[5] or other thiol attaching ligands[45] have been shown to effectively localize to NR ends due to the attachment of CTAB being weaker at the (111) crystalline plane of the NR end[46,67] and increased energetic potential required to remove CTAB from the (250) side facets.[45,46,68] In addition, scanning transmission electron microscopy/ electron energy loss spectroscopy (STEM/EELS) that allows for quantitative measurement of carbon content has shown that the relative binding density of CTAB on the NR is higher at the sides than ends of NRs in a side to end ratio of 1.2 to 1.0 for small NRs, with a reduced ratio of side to end ratio of 1.0 to 1.1 for mini rods,[47] and as CTAB density increases there are more van der Waals interactions between adjacent alkyl chains that make it harder for the ligands to be removed.[16] Thus, confirming that as size increases it becomes easier to displace CTAB since there is a lower density at the ends of NRs when size is larger,[47] allowing for increased ligand replacement during our end coating stage for the larger NRs. This phenomenon is supported by analysis of the Gaussian curvature of each NR size (Figure 6). We would expect that decreasing the size of the NR would increase the correspondent curvature. As discussed by Wu et. al, increasing curvature is correlated with an increased localized ligand density.[69] Thus, the measured curvature values ($1/r^2$ of an inscribed sphere at the tips) of 0.0039 ± 0.0001 nm^{-2}, 0.0050 ± 0.0003 nm^{-2}, 0.013 ± 0.001 nm^{-2}, and 0.020 ± 0.001 nm^{-2} for large, medium, small, and mini rods respectively, is in agreement with the notion that the surface properties at the ends of the NRs facilitate how well self-assembly can occur.

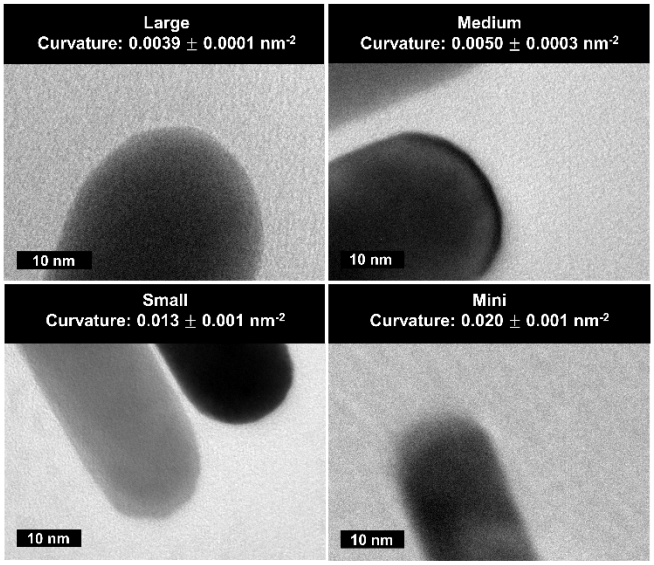

Figure 6. High-resolution TEM images of the ends of each NR size. Scale bars = 10 nm. Gaussian curvature is 0.0039 ± 0.0001 nm^{-2}, 0.0050 ± 0.0003 nm^{-2}, 0.013 ± 0.001 nm^{-2}, and 0.020 ± 0.001 nm^{-2} for large, medium, small, and mini rods respectively.

Analysis of chain length distribution among the different sized NRs shows a larger percentage of longer linkages as the nanorod size increases (Figure 7). (There is a minimal difference between use of a thiol or a disulfide for end-coating the NRs, see Supporting Information). The general trend is that chain lengths of end-to-end assembled NRs increase with absolute NR size. We hypothesize that this trend is controlled by the difference in biotin ligand density at the NR ends, gravitational, and electrostatic forces during the self-assembly process. Acting like a polymerization reaction, directional noncovalent interactions bring the NRs together.[70] Kinetically, forming a NR to NR bond would initially proceed at a quicker rate to form dimers, with trimers, tetramers, and larger chains all gradually requiring more reaction time to occur.[70-72] In suspension, dimerization is the main self-assembly pathway.[44,73-77] However, over time, the NRs begin to sediment out of solution, which would be quicker for larger NRs as well as longer chains of NRs based on faster sedimentation rates.[78] Eckert *et al*. showed the effect of gravitational fields on bulk phase behavior of NRs to cause NRs to layer on top of each other as sedimentation occurs to form sedimentation stacks with the ends most likely vertically.[79] These stacks mimic a top-down approach to self-assembly[13,18,19,21,80-83] using the bottom layer of NRs as the adherent surface to build up the more linkages as gravitational forces bring them down to the bottom[78] and electrostatic forces generate an amplified electric field for in-solution streptavidin to localize and bind to the ends of the NRs for self-assembly of longer chains to occur.[11,84,85]

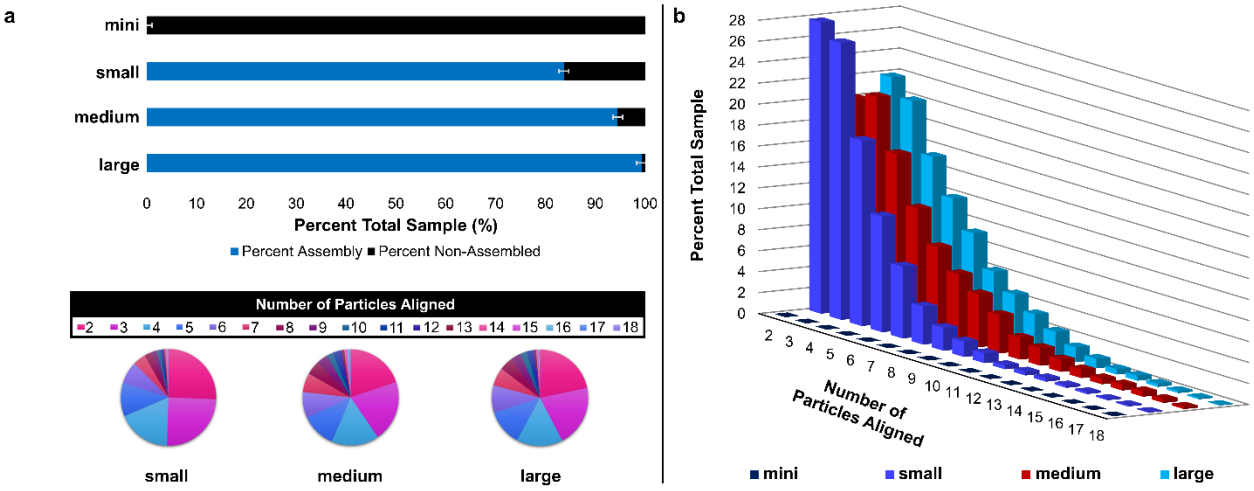

Figure 7. Overall percent assembly of entire sample with number of nanoparticles aligned. (a) Percent of NRs self-assembled versus single NRs with surrounding pie-charts displaying the distribution of multiple self-assembly chain lengths per condition. (b) 3D graph shows side-by-side comparison of distribution between all NR sizes. Error bars represent standard deviation.

Kinetics of the self-assembly process at short times were monitored by extinction spectroscopy (Figure 8a). Intuitively, one may expect that the larger the monomer, the slower the assembly kinetics, just based on diffusion coefficients, per what one may expect for a linear condensation polymer. However, that is not what we observe (Figure 8b). If one monitors the loss of the original monomer longitudinal plasmon band over time (due to monomer consumption, although there will be contributions at that wavelength from

multimers in solution that differ as a function of chain length, as well as any side-to-side assembly; moreover, the linker is large in these experiments, so the plasmonic coupling is more variable than rigid linkers as we have done before), it is observed that the largest change in extinction over short times is from the largest rods, with the small and medium within a factor of two of each other. Since the number of biotins available at the ends of the largest rods is far larger than that of the smaller rods (and it is not clear how many biotin-streptavidin linkages are necessary to cause attachment), comparisons between absolute nanorod sizes for the kinetics become complicated with many possible assumptions that are not well-validated. Therefore, we hesitate to make assumptions that would lead to rigorous rate laws and order of reaction.

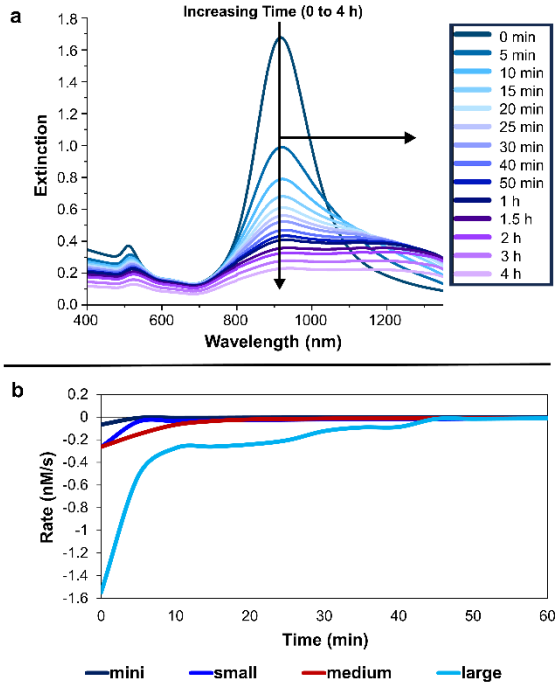

Figure 8. Kinetics of the self-assembly of mini, small, medium, and large NRs, assuming loss of monomer rods over time. (a) *In situ* progression of medium NR self-assembly reaction monitored by UV-Vis over the course of 4 h following streptavidin addition at a 0.125 nM NR concentration. Timepoints were taken every 30 s over the first 5 minutes and every 5 minutes thereafter. (b) Reaction rates over the course of 1 h following the streptavidin addition, considering that the rate is the loss of monomer rods at the plasmon band maximum wavelength.

To further corroborate that size does influence the ability of a NR to self-assemble, we can compare the lack of self-assembly displayed by the mini NR samples (Figure 9). Following the same procedure as with the other sized NRs offered no self-assembly, even after leaving the mini NRs to react over two weeks. Neither relative concentrations, reaction vessel, reaction scale, pH, addition of bovine serum albumin to prevent the NRs from sticking to the walls of the reaction vessel, nor a combination thereof yielded any reactivity other than aggregation. Fully saturating the NRs with streptavidin to ensure interaction and adding sequentially less streptavidin in the event NRs may have been bonded to streptavidin but not each other also yielded no success. The most likely reason for the lack of self-assembly in mini NRs is their more uniform CTAB distribution around the ends vs. the sides,[15] minimizing the disparity between the energy needed to coat either the ends or sides.[45,46,65] Real-time monitoring of the reaction exhibited zero change in concentration of single NRs upon addition of streptavidin, as UV-Vis extinction spectra displayed no shift in LSPR for mini NRs coated with thiol or disulfide for conditions under which assembly would have been expected based on the larger NRs (Figure 9b). Flooding the mini NR samples with biotinylated thiol does

result in some alignment (Figure 9a) with a total percentage of end-to-end linkage of 54.9% out of the combined end-to-end and end-to-side linkages (Figure 4a).

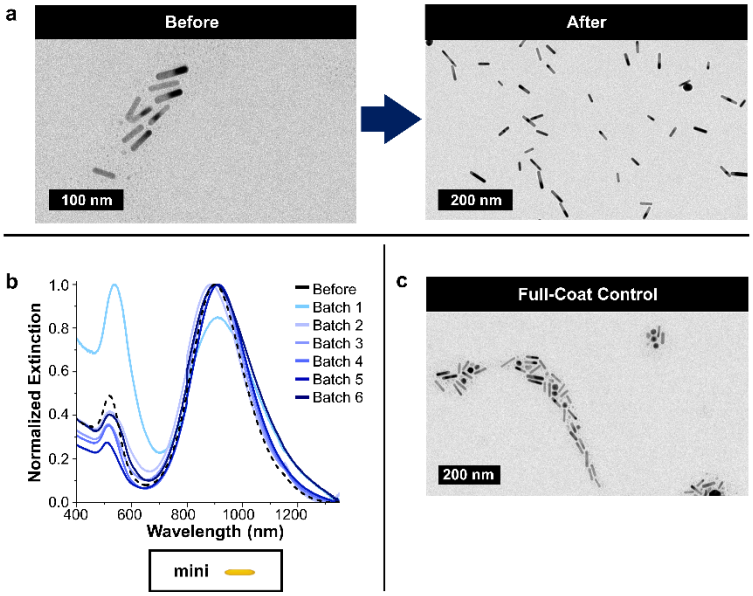

Figure 9. Evidence of mini NRs not undergoing self-assembly upon addition of streptavidin. (a) TEM images of supposed end-coated mini NRs before and after the addition of streptavidin. (b) Extinction spectra of mini NRs before and six representative batches of mini NRs after addition of streptavidin. (c) TEM images of mini NRs fully coated with biotin-PEG-SH after the addition of streptavidin. Scale bars = 100 nm (a, left) and 200 nm (a, right, and c).

Our experimental data support a possible threshold in NR size necessary for NRs to undergo end-to-end self-assembly. We postulate that the differential ligand density between ends and sides of nanorods is responsible for this effect, although intriguing arguments about dipolar and electrostatic forces at the ends of AuNRs may come into play. This aligns with the results found by Valiskó *et al*. during a Monte Carlo simulation (MCS) of hard sphere fluids with extended dipoles.[85] At low densities, such as the ones we used here, the particles' strong dipoles arrange in their minimal energy conformations to form end-to-end chain-like structures. While our system contains more variables in terms of structural and dielectric properties, it is reasoned that the end-to-end attraction between dipoles, repulsion of side-to-side interactions, and the negative energy gained when dipoles are aligned into an end-to-end assembly, seen by Valiskó *et al*. at a partial point charge distance of 0.5 nm, are also in effect for our system. Additionally, Aoshima and Satoh, using sphereocyclinders to represent NRs in a MCS display that particles with strong interactions tend to form clusters through thermodynamic equilibrium via the application of a Markov chain concept.[86] The rods may start out side-by-side in solution, but equilibriate to form end-to-end interactions. Both Aoshima and Satoh[86] and Theiss and Gross[87] expand thermodynamics to uncover that a combination of low density and high dipole moments are necessary for self-assembly to occur. Thus, maintaining the same charge separation and NR length and only changing the NR diameter, increasing aspect ratios cause more end-to-end interactions to occur.[86] This suggests that both NRs with increased surface area at the ends and NRs with increased dipolar energy can increase the potential for self-assembly.

However, since the approach here is bottom-up, relying on ligand-protein interactions for end-to-end assembly rather than electrostatic forces, we infer that our results are mostly due to the spatial dependence of ligand density on AuNRs. For confirmation that the protein streptavidin is indeed in the junctions between the ends of linked nanorods, surface-enhanced Raman scattering (SERS) data were collected on

the final assembled samples. As expected, as the NR size increased, signal intensity increased due to increased electronic field enhancements at the hot-spots where streptavidin was localized.[88-90] Additionally, we once more observed evidence that the mini rods were not undergoing self-assembly, as they showed no signal enhancement of streptavidin and displayed signals characteristic of gold NRs with no streptavidin present (Figure 10).[91] The lack of a SERS effect with the mini rods, as well as the trend of increasing signal strength as NR size increased, corroborates the TEM and extinction data shown earlier.

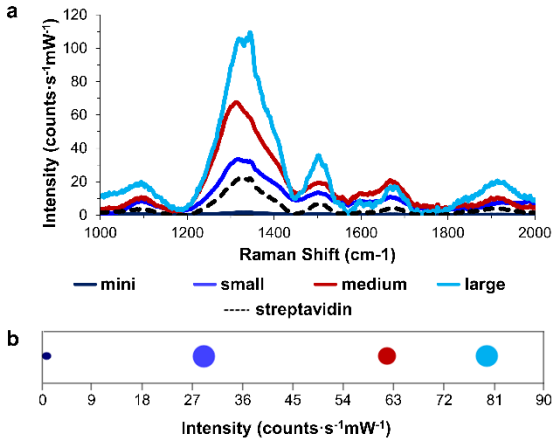

Figure 10. Comparison of SERS amplification of streptavidin signals between all NR sizes. For each condition, six trials were averaged, from AuNR monomer concentrations of 0.125 nM. (a) Stacked SERS data from 1000 to 2000 cm^{-1}. (b) Signal intensity differences at 1295 cm^{-1} (amide III/β-sheet vibrational mode) Raman shift for each condition. Size of plot marker represents range of error.

CONCLUSIONS

End-to-end selective self-assembly of NRs is possible, but herein we have demonstrated significantly improved yields and selectivity by taking advantage of the initial ligand densities of the starting nanorods. We postulate that the lower density of CTAB on the ends of the NRs only makes end-selective functionalization possible above a certain absolute size of NR. We also posit that because CTAB density increases with increasing surface curvature, smaller NRs are more difficult to selectively end-functionalize. In all, we have produced a method for producing high yielding and reliably reproducible bottom-up self-assembly by utilizing the NRs' innate favorability for end functionalization and by not oversaturating the NRs with ligand. We report that size does impact the ability of the NRs to self-assemble by this mechanism, unraveling a part of the enigma surrounding self-assembly of anisotropic nanomaterials. As demonstrated in the analysis of self-assembled NRs, as the size of the NR increases, both the total percentage of NRs in solution that are linked together and the percentage of those assembled NRs participating in chain lengths beyond dimers and trimers significantly increases. Additionally, as displayed by both LSPR shifts and TEM imaging, while small, medium, and large NRs were able to form self-assembled chains, mini NRs resulted in no assembly under numerous conditions, indicating that there exists a minimum size NR needed for end-to-end selective self-assembly to occur.

METHODS/EXPERIMENTAL

Instrumentation.

Nanoparticles were characterized by UV-vis spectroscopy and transmission electron microscopy (TEM). UV-vis spectra were measured with a Cary 5000 UV-vis-NIR spectrophotometer (Agilent Technologies)

over wavelengths 400-1100 nm for CTAB coated nanoparticles and 400-1350 nm for PEGylated nanoparticles. TEM grids (carbon type-B, 300 mesh, copper, Ted Pella) were prepared by dipping the grid in the dispersed nanoparticle solution for 10 minutes, removing grid, and patting grid with a kimwipe. TEM images were collected by a JEOL 2010 LAB6 microscope (JEOL Ltd., Tokyo Japan) in the Frederick Seitz Materials Research Laboratory, Central Facilities at the University of Illinois. Average lengths, widths, and spacing were determined by ImageJ software (National Institutes of Health). For lengths and widths, a minimum of 400 particles were analyzed. For spacing and number of nanoparticles aligned, six separate batches of each condition were analyzed with approximately 16000 nanoparticles per batch and 10000 junctions counted. Inductively coupled plasma mass spectrometry (ICP-MS) was used to determine gold concentrations of each solution using a PerkinElmer Elan DRCe/NexION 350D ICP-MS instrument (PerkinElmer Inc.) in the Microanalysis Laboratory at the University of Illinois School of Chemical Sciences. SERS analyses were conducted using an i-Raman Plus (B&W Tek). HPLC measurements were taken using an Agilent 1290 Infinity II equipped with an Agilent Poroshell 120 column (Agilent Technologies).

Materials and Chemicals.
Chloroauric acid, cetyltrimethylammonium bromide, sodium borohydride, silver nitrate, hydrochloric acid, sodium oleate, sodium hydroxide, hydroquinone, hydrogen peroxide, sodium iodide, iodine, acetonitrile, and methoxy polyethylene glycol thiol (^{m}PEG-SH, molecular weight 2000) were purchased from Millipore Sigma. Biotin-PEG-thiol (molecular weight 2000) was purchased from Biopharma PEG Scientific Inc. Streptavidin was purchased from MedChemExpress. All nanopure water was purified with a Barnstead Nanopure II System (18 MΩ). All denoted concentrations of nanoparticle solutions are based on moles of nanoparticles, not moles of gold.

Synthesis of CTAB-coated mini rods.
The procedure was adapted from Chang et al.[53] A gold seed solution was prepared by adding 0.60 mL of 0.01 M $NaBH_4$ to a stirring solution of 9.75 mL of 0.1 M CTAB and 0.25 mL 0.01 M chloroauric acid. This solution was stirred for 10 minutes and left to sit for 1.5 hours while the growth solution was made. For the growth solution, to 27.00 mL of 0.1 M CTAB with 1.50 mL of chloroauric acid was added 0.60 mL 0.01 M $AgNO_3$. Mixture was inverted 3× to mix, and 0.60 mL of 1.0 N HCl was added. Mixture was inverted 3× to mix, and 0.24 mL 0.1 M ascorbic acid was added. Mixture was inverted 3× to mix, and 3.00 mL of seed solution was added to the growth solution. The reaction was once more inverted 3× and left to age overnight. Reaction was purified via centrifugation (16000 rcf) for 35 minutes, redispersed in water, and centrifuged once more for 35 minutes to yield mini rods (λ = 903 nm, $\varepsilon = 3.50 \times 10^8$ $M^{-1} \cdot cm^{-1}$). Nanorods were characterized using TEM.

Synthesis of CTAB-coated small rods.
The procedure was adapted from Vigderman et al.[54] A gold seed solution was prepared by adding 0.46 mL of 0.01 M $NaBH_4$ in 0.01 M NaOH to a stirring solution of 9.50 mL of 0.1 M CTAB and 0.50 mL 0.01 M chloroauric acid. The solution was stirred for 10 minutes and left to age undisturbed for 2 hours while the growth solution was made. For the growth solution, to 28.50 mL of 0.1 M CTAB and 1.50 mL of chloroauric acid was added 90 µL 0.1 M $AgNO_3$. Mixture was inverted 3× to mix, and 1.50 mL of 0.1 M hydroquinone was added. Mixture was inverted 3× to mix, and 480 µL of seed solution was added to the growth solution. The reaction was once more inverted 3× and left to age overnight. Reaction was purified via centrifugation (4600 rcf) for 30 minutes, redispersed in water, and centrifuged once more for 30 minutes to yield small rods (λ = 938 nm, $\varepsilon = 1.88 \times 10^{10}$ $M^{-1} \cdot cm^{-1}$). Nanorods were characterized using TEM.

Synthesis of CTAB-coated medium rods.
The procedure was adapted from Meyer et al.[15] A gold seed solution was prepared by adding 0.60 mL of 0.01 M $NaBH_4$ to a stirring solution of 9.75 mL of 0.1 M CTAB and 0.25 mL 0.01 M chloroauric acid. This solution was stirred for 10 minutes and left to sit for 2 hours while the growth solution was made. To 1.4887

g of sodium oleate dissolved in 300 mL of 0.1 M CTAB, 28.8 mL of 4 mM $AgNO_3$ was added, and solution stirred for approximately 12 minutes. 300 mL of 1 mM chloroauric acid solution was added, and reaction was left to stir for 1.5 hours, where the color gradually turned from gold to colorless. Then 5.1 mL of 6 M HCl was added and stirred for 10 minutes before stirring was strengthened for the addition of 1.5 mL 64 mM ascorbic acid and 120 μL seed solution. The reaction was left undisturbed for ~16 to 21 h where the solution had turned from colorless to pink in color. Nanorod solutions were transferred to fourteen 50 mL conical tubes, centrifuged for 30 minutes (1500 rcf), supernatant was removed, rods in each tube were redispersed in 5.00 mL of 1 mM CTAB, centrifuged again for 30 minutes (1200 rcf), supernatant was removed, and rods were redispersed in 5.00 mL of 1 mM CTAB. 0.2 M CTAB was then added until the reddish-brown colored rods turned bluish purple. Upon color change, the solution was left to sit overnight, during which the rods accumulated at the bottom of the tube and supernatant containing spherical impurities were removed. The 0.2 M CTAB protocol was repeated on an average of 4 times to provide the cleanest possible sample of medium rods ($\lambda = 918$ nm, $\varepsilon = 2.67 \times 10^{10}$ $M^{-1} \cdot cm^{-1}$). Nanorods were characterized using TEM.

Synthesis of CTAB-coated large rods.
The procedure was adapted from Meyer et al.[15] A gold seed solution was prepared by adding 0.60 mL of 0.01 M $NaBH_4$ to a stirring solution of 9.75 mL of 0.1 M CTAB and 0.25 mL 0.01 M chloroauric acid. This solution was stirred for 10 minutes and left to sit for 2 hours while the growth solution was made. To 1.4887 g of sodium oleate dissolved in 300 mL of 0.1 M CTAB, 28.8 mL of 4 mM $AgNO_3$ was added, and solution stirred for approximately 12 minutes. 300 mL of 1 mM chloroauric acid solution was added, and reaction was left to stir for 1.5 hours, where the color gradually turned from gold to colorless. Then 7.2 mL of 6 M HCl was added and stirred for 10 minutes before stirring was strengthened for the addition of 1.5 mL 64 mM ascorbic acid and 12 μL seed solution. The reaction was left undisturbed for ~16 to 21 h where the solution had turned from colorless to pink in color. Nanorod solutions were transferred to fourteen 50 mL conical tubes, centrifuged for 30 minutes (1000 rcf), supernatant was removed, rods in each tube were redispersed in 5.00 mL of 1 mM CTAB, centrifuged again for 30 minutes (800 rcf), supernatant was removed, and rods were redispersed in 5.00 mL of 1 mM CTAB. 0.2 M CTAB was then added until the reddish-brown colored rods turned bluish purple. Upon color change, the solution was left to sit overnight, during which the rods accumulated at the bottom of the tube and supernatant containing spherical impurities were removed. The 0.2 M CTAB protocol was repeated on an average of 4 times to provide the cleanest possible sample of large rods ($\lambda = 911$ nm, $\varepsilon = 6.96 \times 10^{10}$ $M^{-1} \cdot cm^{-1}$). Nanorods were characterized using TEM.

Nanorod end-functionalization with Biotin-PEG-SH.
For large, medium, and small nanorods, 4.00 mL of a 0.125 nM nanoparticle solution in 0.1 M CTAB was prepared from stock concentrations. To the prepared nanorod solutions, an end-coating solution made up of a 1:1 mixture of biotin-PEG-SH and ^{m}PEG-SH was added, with the amount dependent on the calculated surface area of the ends of each size. For large nanorods, 2.81 μL of 0.50 mM end coating solution was added. For medium nanorods, 2.50 μL of 0.25 mM end coating solution was added. For small nanorods, 2.30 μL of 0.125 mM end coating solution was added. For mini nanorods, 2.53 μL of 0.0125 mM end coating solution was added. After addition of end-coating solution, reaction was placed on an orbital shaker, and agitated for 16 h. Reaction was purified via centrifugation for 30 min for large (800 rcf), medium (1200 rcf), and small (4600 rcf) nanoparticle sizes and 35 min for mini nanoparticles (16000 rcf). Each size was then diluted to 0.125 nM in water.

Nanorod side-functionalization with MeO-PEG-SH.
To a 4.00 mL solution of 0.125 nM end-functionalized nanoparticles in water was added 1.50 mL of 0.50 mM ^{m}PEG-SH., and reaction was placed on an orbital shaker and agitated for 24 h. Upon completion, the reaction was purified via centrifugation for 30 min for large (800 rcf), medium (1200 rcf), and small (4600

rcf) nanoparticle sizes and 35 min for mini nanoparticles (16000 rcf). Each size was then diluted to 0.125 nM in water. UV-Vis and TEM were used to characterize all nanorods before the self-assembly step.

Full-functionalization with Biotin-PEG-SH.
To a 2.00 mL solution of 0.125 nM end-functionalized nanoparticles in water was added 1.00 mL of 0.50 mM biotin-PEG-SH/^{m}PEG-SH solution solution and reaction was placed on an orbital shaker and agitated for 24 h. Upon completion, the reaction was purified via centrifugation for 30 min for large (800 rcf), medium (1200 rcf), and small (4600 rcf) nanoparticle sizes and 35 min for mini nanoparticles (16000 rcf). Each size was then diluted to 0.125 nM in water. UV-Vis and TEM were used to characterize all nanorods before the self-assembly step.

Attempted self-assembly of mini rods.
After subsequent end- and side-functionalization, to a 2.0 mL low-protein-binding microcentrifuge tube (Thermo Fisher Scientific Inc.) was added 1.00 mL of 0.125 nM nanorod solution. 200 μL of 26 nM streptavidin in water was added, reaction was inverted 3 times to mix, and aged undisturbed. Utilizing UV-Vis to monitor the reaction, no self-assembly was observed after 24 h, 48 h, 72 h, 1 week, or 2 weeks. A variety of conditions were investigated in attempt to have the mini rods successfully assemble. Altered reaction concentrations (0.125, 0.25, 0.50, 1.00, 2.50, 5.00, and 10.00 nM), increasing for UV-Vis visibility, resulted in aggregation or no self-assembly. Altered biotin-PEG-SH to ^{m}PEG-SH ratio (1:1, 1:2, 1:3) were utilized during end-functionalizing step for end-functionalization, trialed, and resulted in no self-assembled at any of the seven concentrations. Altered pH through adding a concentration of 1.0 N HCl (0.50, 1.00, 2.00, 3.00, 4.00, 5.00, 7.50, 10.00, 15.00, 20.00, 25.00, 30.00, 40.00, 50.00 and 100.00 μL) or 1.0 N NaOH (0.50, 1.00, , 2.00, 3.00, 4.00, 5.00, 7.50, 10.00, 15.00, 20.00, 25.00, 30.00, 40.00, 50.00 and 100.00 μL) resulted in aggregation or no self-assembly for all concentrations and ratios. Addition of BSA (1.00, 10.00, 100.00, 1000.00 μL) resulted in only aggregation for all concentrations, ratios, and pHs. Variation in amount of 500 nM streptavidin added to each reaction (10.00, 20.00, 30.00, 40.00, 50.00, 60.00, 80.00, and 100.00 μL) did not change results. Each trial was done in triplicate with no yielded success. TEM imaging of select samples confirmed no self-assembly was occurring.

Self-assembly of small rods.
After subsequent end- and side-functionalization, to a 2.0 mL low protein binding microcentrifuge tube (Thermo Fisher Scientific Inc.) was added 1.00 mL of 0.125 nM nanorod solution. 200 μL of 26 nM streptavidin in water was added, reaction was inverted 3× to mix, and aged undisturbed for 24-48 h. UV-Vis and TEM were utilized to assess self-assembly.

Self-assembly of medium rods.
After subsequent end- and side-functionalization, to a 2.0 mL low protein binding microcentrifuge tube (Thermo Fisher Scientific Inc.) was added 1.00 mL of 0.0625 nM nanorod solution. 100 μL of 26 nM streptavidin in water was added, reaction was inverted 3× to mix, and aged undisturbed for 24-48 h. UV-Vis and TEM were utilized to assess self-assembly.

Self-assembly of large rods.
After subsequent end- and side-functionalization, to a 2.0 mL low protein binding microcentrifuge tube (Thermo Fisher Scientific Inc.) was added 1.00 mL of 0.03125 nM nanorod solution. 50 μL of 26 nM streptavidin in water was added, reaction was inverted 3× to mix, and aged undisturbed for 24-48 h. UV-Vis and TEM were utilized to assess self-assembly.

Ligand density quantification
A solution of 13 mg/mL I_2 was dissolved in nanopure water via sonication. To each 1.00 mL of NR solutions were added 1.00 mL of I_2 solution. NRs treated with etchant solution were placed on an orbital shaker for 48 h to ensure complete ligand cleavage. Gold was removed via centrifugation using a 30K Amicron Ultra

0.5 mL centrifugal filter unit (Millipore Sigma) at 5000 rcf for 5 minutes. The filtrate containing the etched off ligands was ran through an Agilent 1290 Infinity II HPLC equipped with an Agilent Poroshell 120 column (C18, 4 μm particle size, 4.6 mm diameter, 100 mm length, PN 69570-902, SN USHKA04056, LN B19079), 100 μL of sample was injected. The sample was subjected to a water and acetonitrile gradient (0-10 min 100% water ramp to 100% acetonitrile, 10-12.5 min hold 100% acetonitrile) for 12.5 minutes at a flow rate of 1.00 mL/min. Eluents was detected using a photo diode array (PDA) set for wavelength detection at 288 nm. The peak area (mAu·s) at the retention time of 8.589 minutes was recorded, corresponding to free ligand. The peak area was converted to concentration using standard calibration curves (1.00, 0.50, 0.25, 0.10, 0.05, 0.025, 0.01, and 0.00 mM biotin-PEG).

Surface curvature analysis

HRTEM images were taken, and a set of six rods per each size were analyzed for Gaussian curvature using the Fiji ImageJ kappa curvature plugin. The output average curvatures of the NR ends were averaged against each other, and standard deviation was obtained amongst the six rods. These values were checked against the measurement of total circular area that encompasses the end of the NR, where $1/r^2$ = Gaussian curvature, to give near identical values. (r = radius)

TEM image analysis

A multitude of TEM images were taken randomly over approximately 75% of each TEM grid. Upon acquisition, TEM images were manually analyzed using ImageJ software. A straight line was lengthened to that of the scale bar to calibrate pixel distance per each image. To perform our measurements, a line was then lengthened to that of the nanorods length, diameter, or the space between two nanorods, depending on the analysis ran, to determine how long, wide, or far apart nanoparticles were. For numerical measurements of length, diameter, and distance between nanorods, the average and standard deviation were calculated for each sample with measurements acquired from six different batches per condition with at least 16,000 NRs and at least 10,000 junctions counted per batch. For the number of NRs aligned, each nanorod assembly was counted manually.

Kinetics measurement

For each NR size, the procedure for self-assembly was undergone in a 1.00 mL quartz cuvette.
Upon streptavidin addition and mixing via pipette, the sample was scanned in the UV-Vis every 30 seconds for the first 5 minutes and every 5 minutes after that for a time span of 4 h. To rule out the factor of nanoparticle sedimentation, controls of just nanoparticle solution without streptavidin were scanned for the 4 hours as well. Rate of change in concentration at the max peak from the control were subtracted from the runs with streptavidin.

Surface-enhanced Raman scattering (SERS) measurements

Following the self-assembly of the NRs with streptavidin, excess streptavidin was removed via centrifugation for 30 min for large (800 rcf), medium (1200 rcf), and small (4600 rcf) nanoparticle sizes and 35 min for mini nanoparticles (16000 rcf). Upon removal of the supernatant containing the excess streptavidin, each NR size was then diluted to 0.125 nM in water. For each measurement, 200 μL aliquots of purified self-assembled solution were added to a glass slide. Then, SERS measurements were performed by placing a glass plate under the Raman objective with the glass slide containing our sample on top of the plate. Measurements were taken using an integration time of 2000000 μs with a spectral averaging of 3, baseline removal, and dark spectral subtraction. The laser was at a wavelength of 785.23 nm at 80% power. For each experimental condition, 6 separate samples were analyzed.

AUTHOR INFORMATION

Corresponding Author

Catherine J. Murphy – Department of Chemistry and Materials Research Laboratory, University of Illinois at Urbana-Champaign, Urbana, Illinois 61801, United States; Urbana−Champaign, Urbana, Illinois 61801, United States; orcid.org/0000-0001-7066-5575; Email: murphycj@ illinois.edu

Author
Maegen Kincanon -Department of Chemistry, University of Illinois at Urbana-Champaign, Urbana, Illinois 61801, United States; orcid.org/0000-0002-1283-9538

Author Contributions
Maegen Kincanon: conceptualization; data cultivation; formal analysis; investigation; methodology; writing – original draft; writing – review and editing. Catherine J. Murphy: conceptualization; funding acquisition; project administration; resources; writing – review and editing.

Notes
The authors declare no competing financial interests.

ACKNOWLEDGEMENTS
This work was supported by the National Science Foundation CHE-2107793.

This research was partially carried out in the Materials Research Laboratory Central Research Facilities at the University of Illinois.

ASSOCIATED CONTENT
Supporting Information
The supporting information is available free of charge at http://pubs.acs.org. Histograms of NR length and diameter homogeneity for each NR size. Representative sets and low magnification TEM images of each self-assembly condition. Trial conditions of failed mini NR self-assembly. Description of detailed methods and analysis pertaining to NR series treated with disulfide-based biotin ligand.

REFERENCES

1. Dey, P.; Baumann, V.; Rodríguez-Fernández, J. Gold Nanorod Assemblies: The Roles of Hot-Spot Positioning and Anisotropy in Plasmon Coupling and SERS. *Nanomaterials* **2020**, *10*, 942.
2. Liang, Z.; Sun, J.; Jiang, Y.; Jiang, L.; Chen, X. Plasmonic Enhanced Optoelectronic Devices. *Plasmonics* **2014**, *9*, 859-866.
3. Pardenkhorram, R.; Bonaccorsi, S.; Zhu, H.; Gonçales, V. R.; Wu, Y.; Liu, J.; Lee, N. A.; Tilley, R. D.; Gooding, J. J. Intrinsic and well-defined second generation hot spots in gold nanobipyramids versus gold nanorods. *Chem. Commun.* **2019**, *55*, 7707-7710.
4. Lin, K.; Yi, J.; Hu, S.; Liu, B.; Liu, J.; Wang, X.; Ren, B. Size Effect on SERS of Gold Nanorods Demonstrated via Single Nanoparticle Spectroscopy. *J. Phys. Chem. C* **2016**, *120*, 20806-20810.
5. Meyer, S. M.; Murphy, C. J. Anisotropic silica coating on gold nanorods boosts their potential as SERS detectors. *Nanoscale* **2022**, *14*, 5214-5226.
6. Tie, L.; Focsan, M.; Bosson, J.; Tira, C.; Campu, A.; Vulpoi, A.; Astilean, S. Controlling the end-to-end assembly of gold nanorods to enhance the plasmonic response in near infrared. *Mater. Res. Express* **2019**, *6*, 095038.
7. Pettine, J.; Meyer, S. M.; Medeghini, F.; Murphy, C. J.; Nesbitt, D. J. Controlling the Spatial and Momentum Distributions of Plasmonic Carriers: Volume vs Surface Effects. *ACS Nano* **2021**, *15*, 1566-1578.
8. Babicheva, V. E.; Zhukovsky, S. V.; Ikhsanov, R. S.; Protsenko, I. E.; Smetanin, I. V.; Uskov, A. Hot Electron Photoemission from Plasmonic Nanostructures: The Role of Surface Photoemission and ransition Absorption. *ACS Photonics* **2015**, *2*, 1039– 1048.

9. Pettine, J.; Marton Menendez, A.; Nesbitt, D. J. Continuous Angular Control over Anisotropic Photoemission from Isotropic Gold Nanoshells. *J. Chem. Phys.* **2020**, *153*, 101101.
10. Imae, T.; Zhang, X. Effect of Au nanorod assemblies on surface-enhanced Raman spectroscopy. *J. Taiwan Inst. Chem. Eng*. **2014**, *45*, 3081-3084.
11. Lenjani, S. V.; Mayer, M.; Wang, R.; Dong, Y.; Fery, A.; Sommer, J.; Rossner, C. Importance of Electrostatic Forces in Supracolloidal Self-Assembly of Polymer-Functionalized Gold Nanorods. *J. Phys. Chem. C.* **2022**, *126*, 14017-14025.
12. Serra, V. V.; Serra, S. G.; Vallejo, M. C. S.; Paulo, P. M. R.; Moura, N. M. M.; Botequim, D.; Neves, M. G. P. M. S.; Costa, S. M. B. Merging Porphyrins with Gold Nanorods: Self-Assembly Construct to High Fluorescent Polyelectrolyte Microcapsules. *Nanomaterials* **2022**, *12*, 872.
13. Nguyen, M. T. T.; Nguyen, D. H.; Pham, M. T.; Pham, H. V.; Huynh, C. D. Synthesis and Vertical Self-Assembly of Gold Nanorods for Surface Enhanced Raman Scattering. *J. Electron. Mater.* **2019**, *48*, 4970-4976.
14. Chen, W.; Roelli, P.; Ahmed, A.; Verlekar, S.; Hu, H.; Banjac, K.; Lingenfelder, M.; Kippenberg, T. J.; Tagliabue, G.; Galland, C. Intrinsic luminescence blinking from plasmonic nanojunctions. *Nature Comm.* **2021**, *12*, 2731.
15. Meyer, S. M.; Pettine, J.; Nesbitt, D. J.; Murphy, C. J. Size Effects in Gold Nanorod Light-to-Heat Conversion under Femtosecond Illumination. *J. Phys. Chem. C* **2021**, *125*, 29, 16268-16278.
16. Lu, M.; Zhu, H.; Hong, L.; Zhao, J.; Masson, J.; Wei, P. Wavelength-Tunable Optical Fiber Localized Surface Plasmon Resonance Biosensor via a Diblock Copolymer Templated Nanorod Monolayer. *ACS Appl. Mater. Interfaces* **2020**, *12*, 50929-50940.
17. Tsargorodska, A.; El Zubir, O.; Darroch, B.; Cartron, M. L.; Basova, T.; Hunter, C. N.; Nabok, A. V.; Leggett, G. J. Fast, Simple, Combinatorial Routes to the Fabrication of Reusable, Plasmonically Active Gold Nanostructures by Interferometric Lithography of Self-Assembled Monolayers. *ACS Nano* **2014**, *8*, 7858-7869.
18. Sharma, Y.; Dhawan, A. Nanoline-gap controlled self assembly of plasmonic nanoparticles inside plasmonic nanolines. *J. Phys. Commun.* **2019**, *3*, 115013.
19. Sikdar, D.; Weir, H.; Kornyshev, A. A. Optical response of electro-tunable 3D superstructures of plasmonic nanoparticles self-assembling on transparent columnar electrodes. *Opt. Express* **2019**, *27*, 26483-26498.
20. Namura, K.; Hanai, S.; Kondo, S.; Kumar, S.; Suzuki, M. Gold Micropetals Self-Assembled by Shadow-Sphere Lithography for Optofluidic Control. Adv. Mater. Interfaces **2022**, 9, 2200200.
21. Lestini, E.; Andrei, C.; Zerulla, D. Linear self-assembly and grafting of gold nanorods into arrayed micrometer-long nanowires on a silicon wafer via a combined top-down/bottom-up approach. *PLoS ONE* **2017**, *13*, e0195859.
22. Dong, J.; Wu, H.; Cao, Y.; Yuan, J.; Han, Q.; Gao, W.; Zhang, C.; Qi, J.; Sun, M. Capillary-force-assisted self-assembly of fold nanoparticles into highly ordered plasmonic thin films for ultrasensitive SERS. *Phys. Chem. Chem. Phys*. **2023**, *25*, 1649-1658.
23. Rycenga, M.; Camargo, P. H. C.; Xia, Y. Template-assisted self-assembly: a versatile approach to complex micro- and nanostructures. *Soft Matter* **2009**, *5*, 1129-1136.
24. Lee, L.; Leite, C. A. P.; Galembeck, F. Controlled Nanoparticle Assembly by Dewetting of Charged Polymer Solutions. *Langmuir* **2004**, *20*, 4430-4435.
25. Abdelrahman, A. I.; Mohammad, A. M.; Okajima, T.; Ohsaka, T. Fabrication and Electrochemical Application of Three-Dimensional Gold Nanoparticles: Self-Assembly. *J. Phys. Chem. B*. **2006**, *110*, 2798-2803.
26. Mayer, M.; Schnepf, M. J.; König, A. F.; Fery, A. Colloidal Self-Assembly Concepts for Plasmonic Metasurfaces. *Adv. Optical Mater*. **2019**, *7*, 1800564.
27. Boles, M. A.; Engel, M.; Talapin, D. V. Self-Assembly of Colloidal Nanocrystals: From Intricate Structures to Functional Materials. *Chem. Rev*. **2016**, *116*, 11220−11289.
28. Grzelczak, M.; Vermant, J.; Furst, E. M.; Liz-Marzán, L. M. Directed Self-Assembly of Nanoparticles. *ACS Nano* **2010**, *4*, 3591-3605.

29. Hughes, R. A.; Menumerov, E.; Neretina, S. When lithography meets self-assembly: a review of recent advances in the directed assembly of complex metal nanostructures on planar and textured surfaces. *Nanotechnology* **2017**, *28*, 282002.
30. Dujardin, E.; Hsin, L.; Wang, C. R. C.; Mann, S. DNA-driven self-assembly of gold nanorods. *Chem. Commun.* **2001**, 1264-1265.
31. Ou, J.; Tan, H.; Chen, X.; Chen, Z. DNA- Assisted Assembly of Gold Nanostructures and Their Induced Optical Properties. *Nanomaterials* **2018**, *8*, 994.
32. Nakamura, S.; Mitomo, H.; Suzuki, S.; Torii, Y.; Sekizawa, Y.; Yonamine, Y.; Ijiro, K. Self-assembly of Gold Nanorods into a Highly Ordered Sheet via Electrostatic Interactions with Double-stranded DNA. *Chem. Lett.* **2022**, *51*, 529-532.
33. He, Z.; Wang, G.; Liang, X.; Takarada, T.; Maeda, M. DNA Base Pair Stacking Assembly of Anisotropic Nanoparticles for Biosensing and Ordered Assembly. *Anal. Sci.* **2021**, *37*, 415-423.
34. Mosquera, J.; Zhao, Y.; Jang, H.; Xie, N.; Xu, C.; Kotov, N. A.; Liz-Marzán, L. M. Plasmonic Nanoparticles with Supramolecular Recognition. *Adv. Funct. Mater.* **2020**, *30*, 1902082.
35. Shanmugam, V.; Chien, Y.; Cheng, Y.; Liu, T.; Huang, C.; Su, C.; Chen, Y.; Kumar, U.; Hsu, H.; Yeh, C. Oligonucleotides-Assembled Au Nanorod-Assisted Cancer Photothermal Ablation and Combination Chemotherapy with Targeted Dual-Drug Delivery of Doxorubicin and Cisplatin Prodrug. *ACS Appl. Mater. Interfaces* **2014**, *6*, 4382-4393.
36. Caswell, K. K.; Wilson, J. N.; Bunz, U. H. F.; Murphy, C. J. Preferential End-to-End Assembly of Gold Nanorods by Biotin-Streptavidin Connectors. J. Am. Chem. Soc. 2003, 123, 13914-13915.
37. Gole, A.; Murphy, C. J. Biotin-Streptavidin-Induced Aggregation of Gold Nanorods: Tuning Rod-Rod Orientation. *Langmuir* **2005**, *21*, 10756-10762.
38. Thomas, K. G.; Barazzouk, S.; Ipe, B. I. I.; Joseph, S. T. S.; Kamat, P. V. Uniaxial Plasmon Coupling through Longitudinal Self-Assembly of Gold Nanorods. *J. Phys. Chem. B.* **2004**, *108*, 13066-13068.
39. Sundeep, P. K.; Joseph, S. T. S.; Thomas, K. G. Selective Detection of Cysteine and Glutathione Using Gold Nanorods. *J. Am. Chem. Soc.* **2005**, *127*, 6516-6517.
40. Hamon, C.; Bizien, T.; Artzner, F.; Even-Hernandez, P.; Marchi, V. Replacement of CTAB with peptidic ligands at the surface of gold nanorods and their self-assembling properties. *J. Colloid. Interface Sci.* **2014**, *424*, 90-97.
41. Zhang, N.; Shen, X.; Lie, K.; Nie, Z.; Kumacheva, E. Polymer-Tethered Nanoparticles: From Surface Engineering to Directional Self-Assembly. *Acc. Chem. Res*. **2022**, *55*, 1503-1513.
42. Lermusiaux, L.; Nisar, A.; Funston, A. M. Flexible synthesis of high-purity plasmonic assemblies. *Nano Research* **2021**, *14*, 635-645.
43. Tan, S. F.; Anand, U.; Mirsaidov, U. Interactions and Attachment Pathways between Functionalized Gold Nanorods. *ACS Nano* **2017**, *11*, 1633-1640.
44. Lu, X.; Punj, D.; Orrit, M. Controlled synthesis of gold nanorod dimers with end-to-end configurations. *RCS Adv.* **2022**, *12*, 13464-13471.
45. Niehues, M.; Tegeder, P.; Ravoo, B. J. Reversible end-to-end assembly of selectively functionalized gold nanorods by light responsive arylazopyrazole-cyclodextrin interaction. *Beilstein J. Org. Chem.* **2019**, *15*, 1407-1415.
46. Carbó-Argibay, E.; Rodríguez-González, B.; Gómez-Graña, S.; Guerrero-Martínez, A.; Pastoriza-Santos, I.; Pérez-Juste, J.; Liz-Marzán, L. M. The Crystalline Structure of Gold Nanorods Revisited: Evidence for Higher-Index Lateral Facets. *Angew. Chem. Int. Ed.* **2010**, *49*, 9397-9400.
47. Janicek, B. E.; Hinman, J. G.; Hinman, J. J.; Bae, S. H.; Wu, M.; Turner, J.; Change, H.; Park, E.; Lawless, R.; Suslick, K. S.; Murphy, C. J.; Huang, P. Y. Quantitative Imaging of Organic Ligand Density on Anisotropic Inorganic Nanocrystals. *Nano Lett.* **2019**, *19*, 6308−6314.
48. Grzelak, D.; Szustakiewicz, P.; Tollan, C.; Raj, S.; Král, P.; Lewandowski, W.; Liz-Marzán, L. M. In Situ Tracking of Colloidally Stable and Ordered Assemblies of Gold Nanorods. *J. Am. Chem. Soc.* **2020**, *142*, 18814-18825.

49. Paulo, P. M. R.; Zijlstra, P.; Orrit, M.; Garcia-Fernandez, M.; Pace, T. C. S.; Viana, A. S.; Costa, S. M. B. End-Specific Functionalization of Gold Nanorods for Plasmonic Biosensing: Effect of Linker Chain Length. *Langmuir* **2017**, *33*, 6503-6510.
50. Chen, H.; Shao, L.; Wang, J. Gold nanorods and their plasmonic properties. *Chem. Soc. Rev.* **2013**, *42*, 2679.
51. Ren, C.; Carvajal, D.; Shull, K. R.; Szleifer, I. Streptavidin-Biotin Binding in the Presence of a Polymer Spaces. A Theoretical Description. *Langmuir* **2009**, *25*, 12283-12292.
52. Thaner, R. V.; Eryazici, I.; Macfarlane, R. J.; Brown, K. A.; Lee, B.; Nguyen, S. T.; Mirkin, C. A. The Significance of Multivalent Bonding Motifs and "Bond Order" in DNA-Directed Nanoparticle Crystallization. *J. Am. Chem. Soc.* **2016**, *138*, 6119-6122.
53. Chang, H.; Murphy, C. J. Mini Gold Nanorods with Tunable Plasmonic Peaks beyond 1000 nm. *Chem Mater.* **2018**, *30*, 1427–1435.
54. Vigderman, L.; Zubarev, E. R. High-Yield Synthesis of Gold Nanorods with Longitudinal SPR Peak Greater than 1200 nm Using Hydroquinone as a Reducing Agent. *Chem. Mater.* **2013**, *25*, 1450–1457.
55. Hinman, J. G.; Eller, J. R.; Lin, W.; Li, J.; Murphy, C. J. Oxidation State of Capping Agent Affects Spatial Reactivity of Gold Nanorods. *J. Am. Chem. Soc.* **2017**, *139*, 29, 9851–9854.
56. Xue, Y.; Li, X.; Li, H.; Zhang, W. Quantifying thiol-gold interactions towards the efficient strength control. *Nat. Commun.* **2014**, *5*, 4348.
57. Dubois, L. H.; Nuzzo, R. G. Synthesis, Structure, and Properties of Model Organic Surfaces. *Annu. Rev. Phys. Chem*. **1992**, *43*, 437-463.
58. Pan, J.; Hu, H. Z. Simulation of CTAB bilayer adsorbed on Au (100), Au (110), and Au (111) surfaces: structure stability and dynamic properties. *J. Chem. Acad. Sci.* **2017**, *34*, 38-49.
59. Thorkelsson, K.; Bai, P.; Xu, T. Self-assembly and applications of anisotropic nanomaterials: A review. *Nano Today* **2015**, *10*, 48-66.
60. Lyu,Y.; Martínez, A.; D'Incà, F.; Mancin, F.; Scrimin, P. The Biotin-Avidin Interaction in Biotinylated Gold nanoparticles and the Modulation of Their Aggregation. *Nanomaterials* **2021**, *11*, 1559.
61. Li, Y.; Zhang, H. Binding of streptavidin to surface-attached biotin with different spacer thicknesses. *J. Wuhan Univ. Technol. Mater. Sci. Ed.* **2015**, *30*, 1304-1309.
62. Gordel, M.; Piela, K.; Kolkowski, R.; Koz'lecki, T.; Buckle, M.; Samoc´, M. End-to-end self-assembly of gold nanorods in isopropanol solution: experimental and theoretical studies. *J. Nanopart. Res.* **2015**, *17*, 477.
63. Jain, P. K.; Eustis, S.; El-Sayed, M. A. Plasmon coupling in nanorod assemblies: optical absorption, discrete dipole approximation simulation, and exciton-coupling model. *J. Phys. Chem. B* **2006**, *110*, 18243–18253.
64. Abtahi, S. M. H.; Burrows, N. D.; Idesis, F. A.; Murphy, C. J.; Saleh, N. B.; Vikesland, P. J. Sulfate-Mediated End-to-End Assembly of Gold Nanorods. *Langmuir* **2017**, *33*, 1486-1495.
65. Jain, P. K.; Lee, K. S.; El-Sayed, I. H.; El-Sayed, M. A. Calculated Absorption and Scattering Properties of Gold Nanoparticles of Different Size, Shape, and Composition: Applications in Biological Imaging and Biomedicine. *J. Phys. Chem. B* **2006**, *110*, 7238-7248.
66. Zijlstra, P.; Paulo, R. M. R.; Xu, Q.; Orrit, M. Chemical Interface Damping in Single Gold Nanorods and Its Near Elimination by End-Specific Functionalization. *Angew. Chem. Int. Ed.* **2012**, *51*, 8352-8355.
67. Choueiri, R. M.; Galati, E.; Klinkova, A.; Thérien-Aubin, H.; Kumacheva, E. Linear assembly of patchy and non-patchy nanoparticles. *Faraday Discuss.* **2016**, *191*, 189-204.
68. Nepal, D.; Park, K.; Vaia, R. A. High-Yield Assembly of Soluble and Stable Gold Nanorod Pairs for High-Temperature Plasmonics. *Small* **2012**, *8*, 1013-1020.
69. Wu, M.; Vartanian, A. M.; Chong, G.; Pandiakumar, A. K.; Hamers, R. J.; Hernandez, R.; Murphy C. J. Solution NMR Analysis of Ligand Environment in Quaternary Ammonium-Terminated Self-

Assembled Monolayers on Gold Nanoparticles: The Effect of Surface Curvature and Ligand Structure. *J. Am. Chem. Soc.* **2019**, *141*, 4316-4327.
70. Klinkova, A.; Thérien-Aubin, H.; Choueiri, R. M.; Rubinstein, M.; Kumacheva, E. K. Colloidal analogs of molecular chain stoppers. *PNAS* **2013**, *110*, 18775-18779.
71. Ferrier Jr., R. C.; Lee, H.; Hore, M. J. A.; Caporizzo, M.; Eckmann, D. M.; Composto, R. J. Gold Nanorod Linking to Control Plasmonic Properties in Solution and Polymer Nanocomposites. *Langmuir* **2014**, *30*, 1906-1914.
72. Scheepers, M. R. W.; Romijn, A. R.; van IJzendoorn, L. J.; Prins, M. W. J. Rate of Dimer Formation in Stable Colloidal Solutions Quantified Using an Attractive Interparticle Force. *Langmuir* **2019**, *35*, 10533-10541.
73. Ni, W.; Mosquera, R. A.; Pérez-Juste, J.; Liz-Marzán, L. M. Evidence for Hydrogen-Bonding-Directed Assembly of Gold Nanorods in Aqueous Solution. *J. Phys. Chem. Lett*. **2010**, *1*, 1181-1185.
74. Sun, Z.; Ni, W.; Yang, Z.; Kou, X.; Li, L.; Wang, J. pH-Controlled Reversible Assembly and Disassembly of Gold Nanorods. *Small* **2008**, *4*, 1287-1292.
75. Liu, J.; Kan, C.; Li, Y.; Ni, Y.; Shi, D. End-to-end and side-by-side assemblies of gold nanorods induced by dithiol poly(ethylene glycol). *Appl. Phys. Lett*. **2014**, *104*, 253105.
76. Zhu, Y.; Kuang, H.; Xu, L.; Ma, W.; Peng, C.; Hua, Y.; Wang, L.; Xu, C. Gold nanorod assembly based approach to toxin detection by SERS. J. *Mater. Chem.* **2012**, *22*, 2387-2391.
77. Stewart, A. F.; Lee, A.; Ahmed, A.; Ip, S.; Kumacheva, E.; Walker, G. C. Rational Design for the Controlled Aggregation of Gold Nanorods via Phospholipid Encapsulation for Enhanced Raman Scattering. *ACS Nano* **2014**, *8*, 5462-5467.
78. Jamison, J. A.; Krueger, K. M.; Yavuz, C. T.; Mayo, J. T.; LeCrone, D.; Redden, J. J.; Colvin, V. L. Size-Dependent Sedimentation Properties of Nanocrystals. *ACS Nano* **2008**, *2*, 311-319.
79. Eckert, T.; Schmidt, M.; de Las Heras, D. Effect of sample height and particle elongation in the sedimentation of colloidal rods. *Soft Matter* **2023**, *19*, 2214-2223.
80. Liu, X.; Yue, X.; Yan, N.; Jiang, W. Self-assembled 3D free-standing superlattices of gold nanoparticles driven by interfacial instability of emulsion droplets. *Mater. Chem. Front.* **2021**, *5*, 7306-7314.
81. Hanske, C.; Tebbe, M.; Kuttner, C.; Bieber, V.; Tsukruk, V. V.; Chanana, M.; König, T. A. F.; Fery, A. Strongly Coupled Plasmonic Modes on Macroscopic Areas via Template-Assisted Colloidal Self-Assembly. *Nano Lett*. **2014**, *14*, 6863-6871.
82. Hamon, C.; Novikov, S.; Scarabelli, L.; Basabe-Desmonts, L.; Liz-Marzán, L. M. Hierarchical Self-Assembly of Gold Nanoparticles into Patterned Plasmonic Nanostructures. *ACS Nano* **2014**, *8*, 10694-10703.
83. Shi, Y.; Li, Q.; Zhang, Y.; Wang, G.; Matsuo, Y.; Liang, X.; Takarada, T.; Ijiro, K.; Maeda, M. Hierarchical growth of Au nanograss with intense built-in hotspots for plasmonic applications. *J. Mater. Chem. C* **2020**, 8, 16073-16082.
84. Taniguchi, Y.; Takishita, T.; Kawai, T.; Nakashima, T. End-to-End Self-Assembly of Semiconductor Nanorods in Water by Using an Amphiphilic Surface Design. *Angew. Chem. Int. Ed.* **2016**, *55*, 2083-2086.
85. Valiskó, M.; Varga, T.; Baczoni, A.; Boda, D. The structure of strongly dipolar hard sphere fluids with extended dipoles by Monte Carlo simulations. *Mol. Phys.* **2010**, *108*, 87-96.
86. Aoshima, M.; Satoh, A. Two-dimensional Monte Carlo simulations of a colloidal dispersion composed of rod-like ferromagnetic particles in the absence of an applied magnetic field. *J. Colloid Interface Sci.* **2006**, *293*, 77-87.
87. Theiss, M.; Gross, J. Dipolar Hard Spheres: Comprehensive Data from Monte Carlo Simulations. *J. Chem. Eng. Data* **2019**, *64*, 827-832.
88. Galarreta, B. C.; Norton, P. R.; Lagugné-Labarthet, F. SERS Detection of Streptavidin/Biotin Monolayer Assemblies. *Langmuir* **2011**, *27*, 1494-1498.

89. Chen, T.; Wang, H.; Chen, G.; Wang, Y.; Feng, Y.; Teo, W. S.; Wu, T.; Chen, H. Hotspot-Induced Transformation of Surface-Enhanced Raman Scattering Fingerprints. *ACS Nano* **2010**, *4*, 3087-3094.
90. Benz, F.; Chikkaraddy, R.; Salmon, A.; Ohadi, H.; de Nijs, B.; Mertens, J.; Carnegie, C.; Bowman, R. W.; Baumberg, J. J. SERS of Individual Nanoparticles on a Mirror: Size Does Matter, but so Does Shape. *J. Phys. Chem. Lett.* **2016**, *7*, 2264-2269.
91. Rutherford, G.; Xiao, B.; Carvajal, C.; Farrell, M.; Santiago, K.; Cashwell, I.; Pradhan, A. Photochemical Growth of Highly Densely Packed Gold Nanoparticle Films for Biomedical Diagnostics. *ECS J. Solid State Sci. Technol.* **2015**, *4*, S3071-S3076.